Attenuation in waveguides on FR-4 boards due to periodic substrate undulations

Yin-Jung Chang, Thomas K. Gaylord, and Gee-Kung Chang

The guided-mode attenuation associated with optical-interconnect-polymer waveguides fabricated on FR-4 printed-circuit boards is quantified. The rigorous transmission-line network approach is used and the FR-4 substrate is treated as a long-period substrate grating. A quantitative metric for an appropriate matrix truncation is presented. The peaks of attenuation are shown to occur near the Bragg conditions that characterize the leaky-wave stop bands. For a typical 400 μm period FR-4 substrate with an 8 μm corrugation depth, a buffer layer thickness of about 40 μm is found to be needed to make the attenuation negligibly small.

OCIS codes: 050.0050, 130.2790.

1. Introduction

Board-level guided-wave optical interconnects are of growing interest for boosting chip-to-chip transmission data rates that are currently limited by the aspect ratio of the metal interconnects,[1] frequency-dependent dielectric loss, and signal integrity demands in multigigahertz frequency range.[2] Various board-level optical interconnects using guided-wave configurations have been proposed and extensively investigated, including fully embedded optical interconnects,[3,4] fully surface-mount-technology-compatible optical-I/O package,[5] on-board optical interconnects with planarized board surfaces,[6] and Optochips assembled directly on an organic card with integrated parallel waveguides.[7] Among these various structure configurations, polymer waveguides were either laminated inside the printed-circuit boards[3–5] (PCB) or fabricated on top of the signal plane of the board.[6,7] In either case, a buffer and/or cladding layer is necessary to separate the polymer-based waveguide core material from the surrounding PCB substrate and the surface undulations of the FR-4 PCB.

Though no further information on the buffer or cladding layer thickness was given for embedded and on-board optical layers reported,[3–5,7] Chang *et al.*[6] did address the importance of the surface planarization for polymer waveguide fabrication on inexpensive FR-4 PCBs. The thickness of the buffer layer reported[6] is approximately 30 μm after the final curing process. The need for a thick buffer layer is due to the surface undulation and local surface roughness found in FR-4 PCBs. Most FR-4 bare boards have ±2 to ±4 μm undulation with period of 400 to 800 μm and local roughness of ±0.4 to ±0.5 μm. The undulation arises from the woven fiberglass buried inside the board for reinforcement, as can be seen in the C-mode scanning acoustic microscope (C-SAM) photography shown in Fig. 1. A local roughness that is greater than 25 nm will cause optical scattering losses.[6] However, no further analysis and explanation regarding the effect of the long-period FR-4 substrate undulations on the guided-mode(s) propagation have been discussed.

As far as the long-period undulations are concerned, a structure similar to the dielectric waveguide on periodic FR-4 substrate is the long-period waveguide grating (LPWG). Since being proposed,[8] LPWG notch filters with corrugations formed on the waveguide core surface have been experimentally demonstrated.[9–13] They operate by coupling the fundamental guided mode to a particular leaky cladding mode at the wavelength specified by the phase-matching condition[8,14]

$$\lambda_0 = (N_0 - N_m)\Lambda, \tag{1}$$

where λ_0 is the resonance wavelength, Λ is the grating period, and N_0 and N_m are the modal indices of the fundamental mode and the mth cladding mode, respectively. In contrast to the core-corrugation configura-

The authors are with the School of Electrical and Computer Engineering, Georgia Institute of Technology, Atlanta, Georgia 30332, USA. Y.-J. Chang's e-mail address is yjchang@ece.gatech.edu.

Received 11 September 2006; accepted 25 October 2006; posted 1 December 2006 (Doc. ID 74902); published 3 April 2007.
0003-6935/07/122234-10$15.00/0

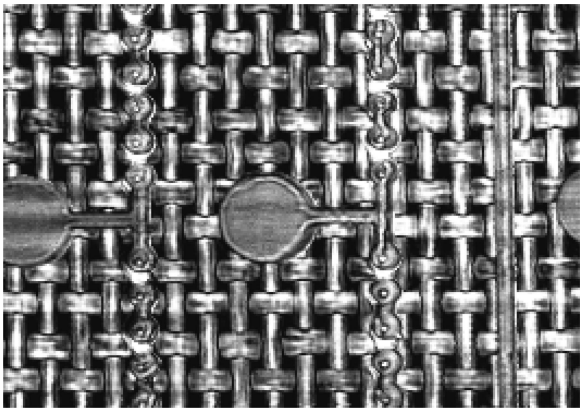

Fig. 1. Three-dimensional C-SAM image of the interior structure of a high-density built-up interconnect board. Copper lines, bonding pads, vias, and woven glass fiber are clearly visible.

tion, Tsoi *et al.*[15] and Perentos *et al.*[16] demonstrated another type of LPWG notch filter where the corrugated buffer layer and/or substrate with a channel waveguide[15] or a raised rib waveguide[16] was fabricated. The phase-matching condition was reported to be satisfied in this type of structure.

Two features of a dielectric waveguide on an FR-4 PCB with long-period substrate undulations that distinguish it from the LPWGs described above are as follows: (1) The corrugation is on the substrate surface and can be retained on the buffer layer, depending on the starting structure of the FR-4 substrate. (2) The on-board polymer waveguide is, in general, multimode, rather than single mode. In addition, previously reported LPWGs were all treated as a perturbation to a uniform waveguide. The refractive index modulation was achieved either through a small corrugation depth (usually <150 nm) (Refs. 9–12) or a thermooptic index perturbation induced by periodic heaters.[13] Accordingly, conventional coupled-mode theory has been applied to analyze the transmission spectra of LPWGs.[8,14,17] The phase-matching condition derived from the coupled-mode theory is a special form of the Floquet condition. Thus for a larger corrugation depth and/or larger refractive index modulation, the modal indices need to be rigorously determined within the context of the boundary-value problem. The modal indices in the presence of such gratings will differ from those of the unperturbed case where the grating structures are absent.

In this paper, we analyze possible large attenuations of an on-board slab waveguide resulting from the long-period FR-4 straight ($\epsilon_r = 4.4$–4.6) substrate undulations. The rigorous transmission-line network approach is applied to the long-period case for the first time. The present research also provides a quantitative estimate of and physical insights to the buffer layer thickness required to planarize the FR-4 surface so that the attenuation can be made negligibly small.

2. Method of Analysis

To address the electromagnetic problem posed by the periodic cladding and substrate surface, the general geometry shown in Fig. 2 is considered. This geometry may contain an arbitrary number of uniform and periodic dielectric layers, each of which is labeled by the index i with a corresponding thick-

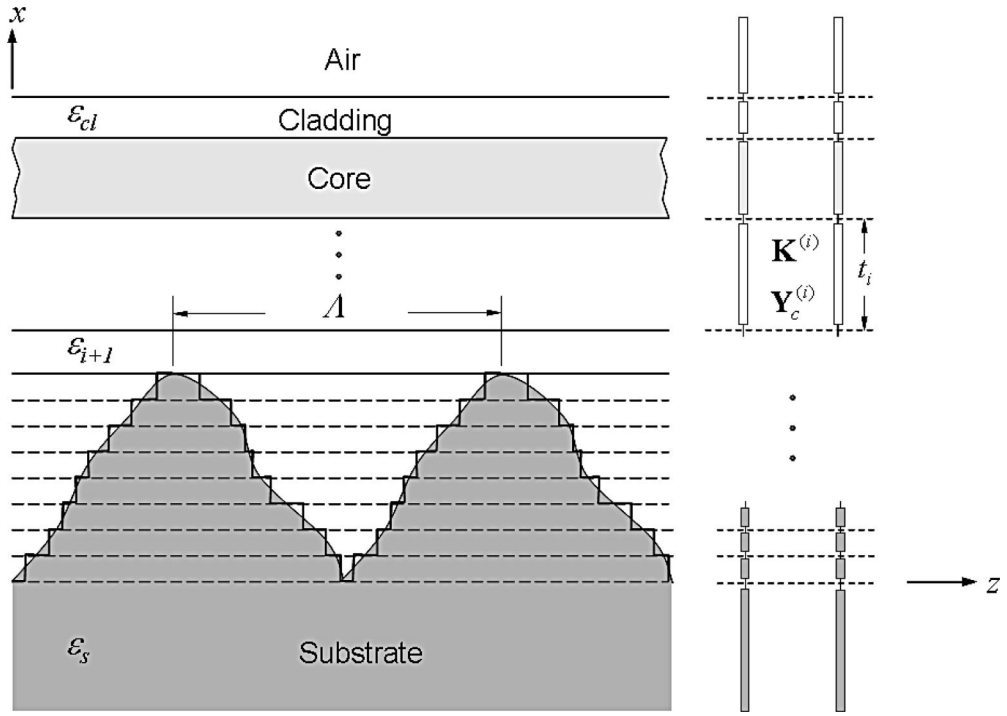

Fig. 2. General geometry and the associated transmission-line network for the analysis of guided-mode attenuation due to long-period substrate and cladding grating.

ness of t_i. The periodic cladding and/or substrate surface with an arbitrary profile is treated as a stack of one-dimensional (1D) periodic sublayers, each of which has a stepwise varied permittivity with respect to z. The permeability in the entire structure is assumed to be the permeability of free space μ_0 and the time-harmonic dependence $\exp(j\omega t)$ is suppressed. Also, the local coordinate associated with each layer $\{0 < x_i < t_i; x_i \in$ the ith layer$\}$ is used. For a 2D geometry ($\partial/\partial y = 0$), the fields in the ith layer can be decomposed into TE and TM modes. For TE modes,

$$E_y^{(i)}(x, z) = \sum_n V_n^{(i)\prime}(x)\exp(-jk_{zn}z), \tag{2a}$$

$$H_x^{(i)}(x, z) = \sum_n -G_n^{(i)\prime}(x)\exp(-jk_{zn}z), \tag{2b}$$

$$H_z^{(i)}(x, z) = \sum_n I_n^{(i)\prime}(x)\exp(-jk_{zn}z). \tag{2c}$$

For TM modes,

$$H_y^{(i)}(x, z) = \sum_n -I_n^{(i)\prime\prime}(x)\exp(-jk_{zn}z), \tag{3a}$$

$$E_x^{(i)}(x, z) = \sum_n -G_n^{(i)\prime\prime}(x)\exp(-jk_{zn}z), \tag{3b}$$

$$E_z^{(i)}(x, z) = \sum_n V_n^{(i)\prime\prime}(x)\exp(-jk_{zn}z), \tag{3c}$$

where $V_n(x)$, $G_n(x)$, and $I_n(x)$ represent the transverse field variations of the nth mode, while primed and double primed symbols denote the fields that apply for TE and TM modes, respectively. In the presence of the periodic boundary, the field solutions must be of the Floquet form[18]:

$$k_{zn} = k_{z0} + n\frac{2\pi}{\Lambda}, \quad n = \{0, \pm 1, \pm 2, \ldots\}. \tag{4}$$

Here k_{zn} is the complex propagation constant with $k_{z0} = \beta_0 - j\alpha$ being the fundamental longitudinal propagation factor, n is the space harmonic order, and Λ is the period of the periodic boundary. The real part of k_{zn} is the phase constant of the nth space harmonic, and the imaginary part α ($\alpha > 0$) is the attenuation constant accounting for the leakage of guided-mode energy from the waveguide core layer. Modal voltage $V_n^{(i)}(x)$ and modal current $I_n^{(i)}(x)$ in the uniform layer satisfy the transmission-line equations that have been explained in detail in the previous literature.[18,19]

Although the general field solutions in the rectangular surface-relief grating region have been derived and described extensively,[18–22] here we present in a clear and systematic manner the formulations of the general field solutions in the grating region by starting from the differential form of the two Maxwell curl equations, $\nabla \times \vec{E} = -j\omega\mu_0\vec{H}$ and $\nabla \times \vec{H} = j\omega\epsilon_0\epsilon(z)\vec{E}$, in the 1D periodic layer.

The periodic permittivity $\epsilon_i(z)$ of the ith grating layer can be expressed as a Fourier series expansion[18]:

$$\epsilon_i(z) = \sum_p c_p^{(i)} \exp(j2p\pi/\Lambda), \tag{5}$$

where $c_p^{(i)}$ is the Fourier coefficient for a given grating profile. For TE modes, substituting the field expressions in Eqs. (2) and (5) into the Maxwell curl equations yields the following system of three coupled equations:

$$\frac{d\underline{V}^{(i)\prime}(x)}{dx} = -jw\mu_0\underline{I}^{(i)\prime}(x), \tag{6}$$

$$\mathbf{k}_z'\underline{V}^{(i)\prime}(x) = w\mu_0\underline{G}^{(i)\prime}(x), \tag{7}$$

$$\frac{-d\underline{I}^{(i)\prime}(x)}{dx} + j\mathbf{k}_z'\underline{G}^{(i)\prime}(x) - jw\epsilon_0\mathbf{C}^{(i)}\underline{V}^{(i)\prime}(x) = 0. \tag{8}$$

Here $\underline{V}^{(i)\prime}(x)$, $\underline{I}^{(i)\prime}(x)$, and $\underline{G}^{(i)\prime}(x)$ are column vectors, $\mathbf{k}_z'$ is a diagonal matrix with entries $(\mathbf{k}_z')_{kl} = k_{zn}'\delta_{kl}$, and $\mathbf{C}^{(i)}$ is the square matrix with elements $c_{kl} = c_{k-l}$, $k - l = p$, where index p is defined in Eq. (5). Substituting Eqs. (6) and (7) into Eq. (8), a system of differential equations for the modal voltages is obtained as

$$\frac{-d^2\underline{V}^{(i)\prime}(x)}{dx^2} = \mathbf{\Delta}^{(i)}\underline{V}^{(i)\prime}(x), \tag{9}$$

where

$$\mathbf{\Delta}^{(i)} \equiv k_0^2\mathbf{C}^{(i)} - (\mathbf{k}_z')^2. \tag{10}$$

Equation (10) characterizes the coupling between all of the space harmonics in the ith grating region. The modal voltages $\underline{V}^{(i)\prime}(x)$ and currents $\underline{I}^{(i)\prime}(x)$ associated with the ith grating layer are obtained as

$$\underline{V}^{(i)\prime}(x) = \mathbf{Q}^{(i)}\Big[\exp\Big(-j\sqrt{\mathbf{\Lambda}^{(i)}}x\Big)\underline{V}^{(i)\prime+} + \exp\Big(j\sqrt{\mathbf{\Lambda}^{(i)}}x\Big)\underline{V}^{(i)\prime-}\Big], \tag{11a}$$

$$\underline{I}^{(i)\prime}(x) = \mathbf{Q}^{(i)}\frac{\sqrt{\mathbf{\Lambda}^{(i)}}}{\omega\mu_0}\Big[\exp\Big(-\sqrt{\mathbf{\Lambda}^{(i)}}x\Big)\underline{V}^{(i)\prime+} - \exp\Big(j\sqrt{\mathbf{\Lambda}^{(i)}}x\Big)\underline{V}^{(i)\prime-}\Big], \tag{11b}$$

where $\mathbf{Q}^{(i)}$ is a square matrix composed of the eigenvectors of $\mathbf{\Delta}^{(i)}$, and $\mathbf{\Lambda}^{(i)}$ is the diagonal matrix with the entries being the corresponding eigenvalues. Hence $\big(\sqrt{\mathbf{\Lambda}^{(i)}}\big)_{kk}$ is the transverse propagation constant associated with the kth independent mode propagating in the x direction. For TM modes, the system of differential equations for the modal currents can be obtained in a similar manner as

$$\frac{-d^2\underline{\mathbf{I}}^{(i)\prime\prime}(x)}{dx^2} = \mathbf{\Omega}^{(i)}\underline{\mathbf{I}}^{(i)\prime\prime}(x), \tag{12}$$

where

$$\mathbf{\Omega}^{(i)} \equiv \mathbf{C}^{(i)}\left\{k_0^2\mathbf{I} - (\mathbf{k}_z'')\mathbf{C}^{(i)^{-1}}(\mathbf{k}_z'')\right\}, \tag{13}$$

with $\mathbf{I}$ being the identity matrix. The modal current and the modal voltage column vectors are thus given by

$$\underline{\mathbf{I}}^{(i)\prime\prime}(x) = \mathbf{P}^{(i)}\left[\exp\left(-j\sqrt{\mathbf{D}^{(i)}}x\right)\underline{\mathbf{I}}^{(i)\prime\prime+} - \exp\left(j\sqrt{\mathbf{D}^{(i)}}x\right)\underline{\mathbf{I}}^{(i)\prime\prime-}\right], \tag{14a}$$

$$\underline{\mathbf{V}}^{(i)\prime\prime}(x) = \mathbf{C}^{(i)^{-1}}\mathbf{P}^{(i)}\frac{\sqrt{\mathbf{D}^{(i)}}}{\omega\epsilon_0}\left[\exp\left(-j\sqrt{\mathbf{D}^{(i)}}x\right)\underline{\mathbf{I}}^{(i)\prime\prime+} + \exp\left(j\sqrt{\mathbf{D}^{(i)}}x\right)\underline{\mathbf{I}}^{(i)\prime\prime-}\right], \tag{14b}$$

where $\mathbf{P}^{(i)}$ is a square matrix composed of the eigenvectors of $\mathbf{\Omega}^{(i)}$ and $\mathbf{D}^{(i)}$ is the diagonal matrix with entries being the corresponding eigenvalues. The input–output relations, including the reflectance matrix at the output end ($\mathbf{\Gamma}_{out}$), the input impedance matrix seen looking toward the output end at $x = x_i$ [$\mathbf{Z}_{in}(x_i)$], and the transfer matrices of the modal voltages [$\mathbf{T}_V(t_i)$] and currents [$\mathbf{T}_I(t_i)$] associated with the ith layer, can therefore be derived based on Eqs. (11) and (14).

For the guided-wave problem, the complex fundamental propagation constant k_{z0} is of interest. It must be numerically obtained by solving the dispersion relation,

$$\det\{\mathbf{Z}_{up} + \mathbf{Z}_{dn}\} = 0, \tag{15}$$

which is the condition for the existence of a nontrivial solution to the boundary-value problem when the incident wave is absent. Quantities $\mathbf{Z}_{up}$ and $\mathbf{Z}_{dn}$ represent the input impedance seen looking upward and downward from the reference plane, respectively. They can be readily obtained by applying the input–output relations layer-by-layer subject to the continuity condition on the tangential electric (modal voltage) and the magnetic (modal current) fields at each layer interface. Hence $\mathbf{Z}_{in}^{(i)}(x_i^-) = \mathbf{Z}_{out}^{(i+1)}(x_i^+)$ holds for every interface between adjacent layers, where $\mathbf{Z}_{in}^{(i)}(x_i^-)$ is the input impedance seen looking downward at $x = x_i^-$ by the ith layer and $\mathbf{Z}_{out}^{(i+1)}(x_i^+)$ is the output impedance seen looking downward at $x = x_i^+$ by the $(i + 1)$th layer. The equivalent transmission-line network associated with either a uniform region or a grating region is characterized by its own characteristic impedance and admittance matrices

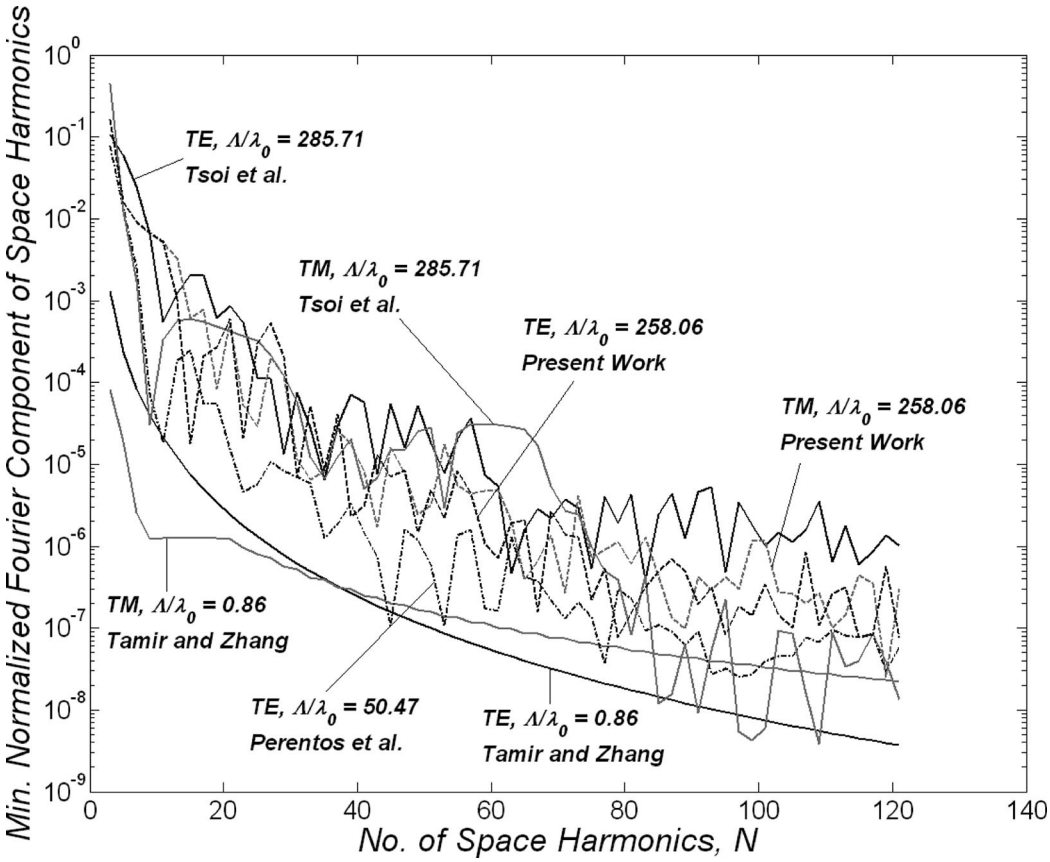

Fig. 3. Minimum normalized amplitude of space harmonics in the grating layer as a function of the number of space harmonics used in the numerical computations.

($\mathbf{Z}_c^{(i)} = \mathbf{Y}_c^{(i)^{-1}}$), complex propagation constant matrix $\left[\mathbf{K}^{(i)}\right.$ with $(\mathbf{K}^{(i)})_{kl} = \left(\sqrt{k_0^2\epsilon_i - k_{zn}^2}\right)\delta_{kl}$, $\sqrt{\mathbf{\Lambda}^{(i)}}$, or $\left.\sqrt{\mathbf{D}^{(i)}}\right]$, and/or the amplitude matrix of space harmonics ($\mathbf{Q}^{(i)}$ or $\mathbf{P}^{(i)}$). Directly applying the continuity of modal voltages and currents based on Eqs. (11) and (14) facilitates the cascade of transmission-line networks without introducing interface transformers when cascading a uniform layer to a grating layer.

3. Computational Considerations and Verifications

The electromagnetic model developed was verified by checking the power conservation associated with the plane-wave scattering problem,

$$\sum_i \underline{P}_r + \underline{P}_t = 1, \tag{16}$$

where $\underline{P}_r$ and $\underline{P}_t$ are the reflected and transmitted power vectors at the air-dielectric interface, respectively:

$$\underline{P}_r = \mathrm{Re}\{|\underline{V}_r^{(inc)}\underline{V}_r^{(inc)}|\underline{Y}_c^{(inc)}\}/\mathrm{Re}\{\underline{P}_{inc}\}, \tag{17a}$$

$$\underline{P}_t = \mathrm{Re}\{|\underline{V}_t^{(inc)}\underline{V}_t^{(inc)}|\underline{Y}_c^{(out)}\}/\mathrm{Re}\{\underline{P}_{inc}\}, \tag{17b}$$

with $\underline{V}_r^{(inc)} = \mathbf{\Gamma}^{(inc)}\underline{V}_{inc}$, $\underline{V}_t^{(inc)} = \mathbf{T}^{(inc)}\underline{V}_{inc}$, $\underline{P}_{(inc)} = \mathrm{Re}\{|\underline{V}_{inc}\underline{V}_{inc}|\underline{Y}_c^{(inc)}\}$ being the reflected voltage vector ($\underline{V}_r^{(inc)}$), transmitted voltage vector ($\underline{V}_t^{(inc)}$), and the incident power vector ($\underline{P}_{inc}$) in the incident region, respectively. Equation (16) must be satisfied for any number of space harmonics used in the field expansion.

Since the transmission-line network approach involves matrices that are, in general, infinite, they must be judiciously truncated for accurate numerical computations. Using intuitive arguments, a simple criterion for the truncation size N has been proposed by retaining a number of evanescent harmonics on each side of propagating orders.[19] To establish a mathematically rigorous yet simple cri-

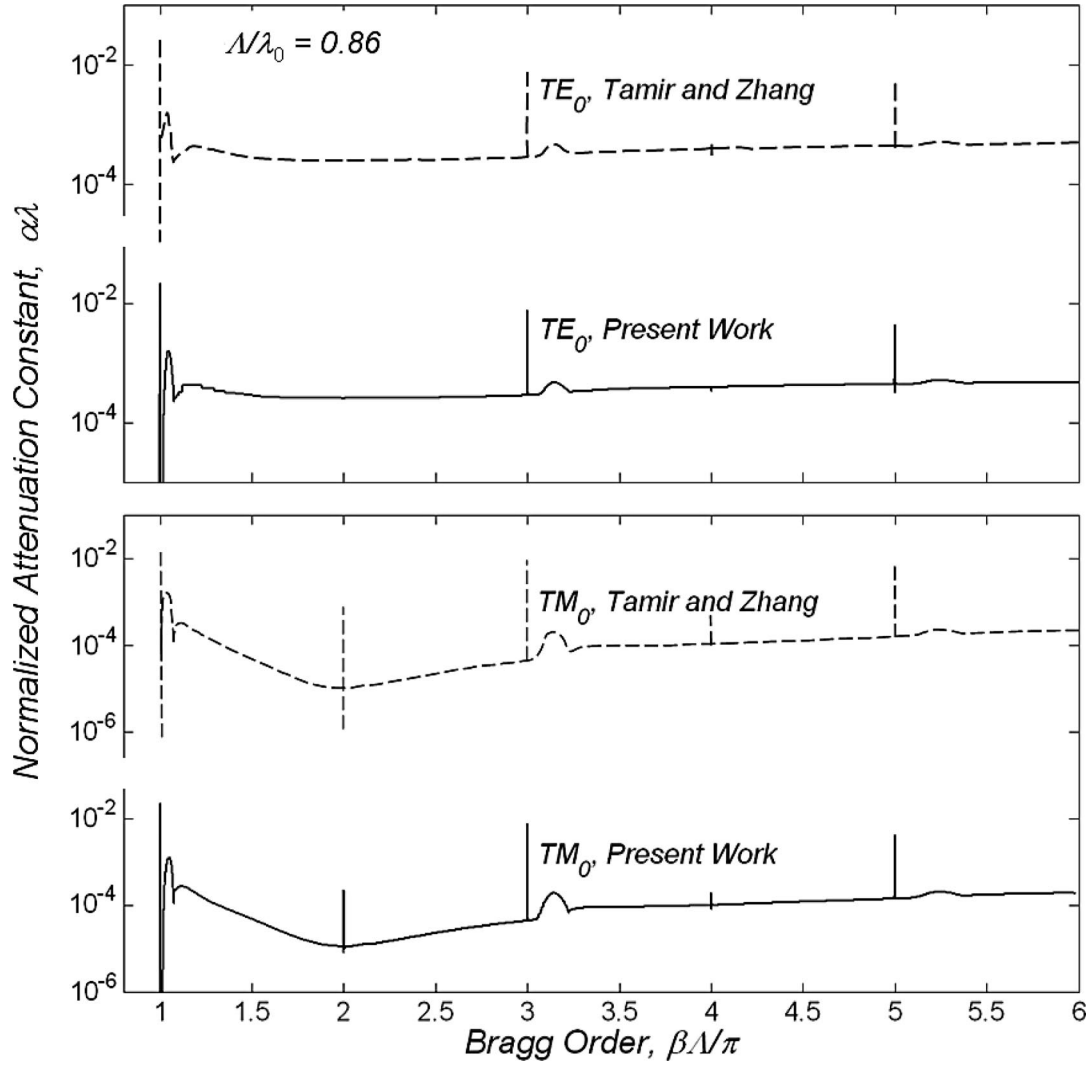

Fig. 4. Comparisons between the present dispersion curves for TE_0 mode and TM_0 mode and those of Tamir *et al.* (Ref. 19). The variable α is the attenuation constant while λ is the operating wavelength.

terion for the matrix truncation, the minimum normalized amplitude of space harmonics is used as a metric. Recalling that the matrices $\mathbf{Q}^{(i)}$ and $\mathbf{P}^{(i)}$ are composed of the amplitude of each space harmonic in the grating region, the minimum normalized amplitude of space harmonics would represent the significance of the highest order retained in the computation. Figure 3 shows this metric versus the number of space harmonics for cases having differing values of normalized period Λ/λ_0. These cases include the structures treated by Tamir *et al.* ($\Lambda/\lambda_0 = 0.86$),[19] Perentos *et al.* ($\Lambda/\lambda_0 = 50.47$),[16] Tsoi *et al.* ($\Lambda/\lambda_0 = 285.71$),[15] and the present FR-4 case ($\Lambda/\lambda_0 = 258.06$). In general, the minimum normalized amplitude decreases as the number of space harmonics increases. This indicates the contribution from higher-order space harmonics (and equivalently, the independent transverse modes) to the total fields would become less significant and can thus be neglected. For example, for the $\Lambda/\lambda_0 = 0.86$ case, <20 space harmonics are sufficient to obtain a value of 10^{-5} for the minimum normalized amplitude of space harmonics. As the Λ/λ_0 value increases to 50.47 and 258.06, the respective number of space harmonics needed becomes at least 27 and 41 for the criterion of 10^{-5}. Also, the relation between the Λ/λ_0 value and the number of space harmonics needed follows a natural logical progression. Moreover, it appears that more space harmonics are needed for TM polarization for large Λ/λ_0 values (258.06 and 285.71). Extensive effort was made to verify the validity of the proposed truncation criterion. The results show that this approach offers a good estimate for the starting number of the space harmonics needed for convergence.

For guided-wave problems, the modified secant version of the complex Newton's method was applied to find the complex roots of the dispersion relation

$$\begin{bmatrix}(\beta-\beta_1)\\(\alpha-\alpha_1)\end{bmatrix}=\frac{\begin{bmatrix}\mathrm{Im}\{(\partial F/\partial\alpha)^*F\}\\-\mathrm{Im}\{(\partial F/\partial\beta)^*F\}\end{bmatrix}}{\mathrm{Im}\left\{\left(\frac{\partial F}{\partial\beta}\right)\left(\frac{\partial F}{\partial\alpha}\right)^*\right\}},\tag{18}$$

where β_1 and α_1 are the real and imaginary parts of the initial value in each iteration, respectively, F represents the complex-valued function defined as $F \equiv \det(\mathbf{Z}_{up} + \mathbf{Z}_{dn})$, the asterisk denotes the complex conjugate, and $\mathrm{Im}(\xi)$ is the imaginary part of a complex number ξ. To verify the validity and the effectiveness of this modified complex Newton's method, we repeat the results reported by Tamir *et al.*[19] Figure 4 illustrates the comparisons of dispersion curves between the present computations and those in Tamir *et al.*[19] They are essentially identical. The number of space harmonics employed, also known as the truncation order, in the present work is 13 for TE and 21 for TM for accuracy to seven significant figures, as opposed to 27 for TE and 77 for TM with $\Lambda/\lambda_0 \leq 2$ reported previously. This comparison validates the model developed and the complex root-finding algorithm for further investigations on structures involving long-period substrate gratings.

4. Computational Results and Discussions

Before the extensive numerical computations for the FR-4 case, comparisons were made with published experimental results and the convergence test of the attenuation constant against the number of space harmonics employed for the FR-4 substrate undulations was carried out. Figure 5 shows the comparison of computational result with the experimental data in Perentos *et al.*[16] The structure under investigation is a 1 cm long long-period waveguide grating with a grating depth of 0.1 μm and a period of 80 μm fabricated on the surface of a

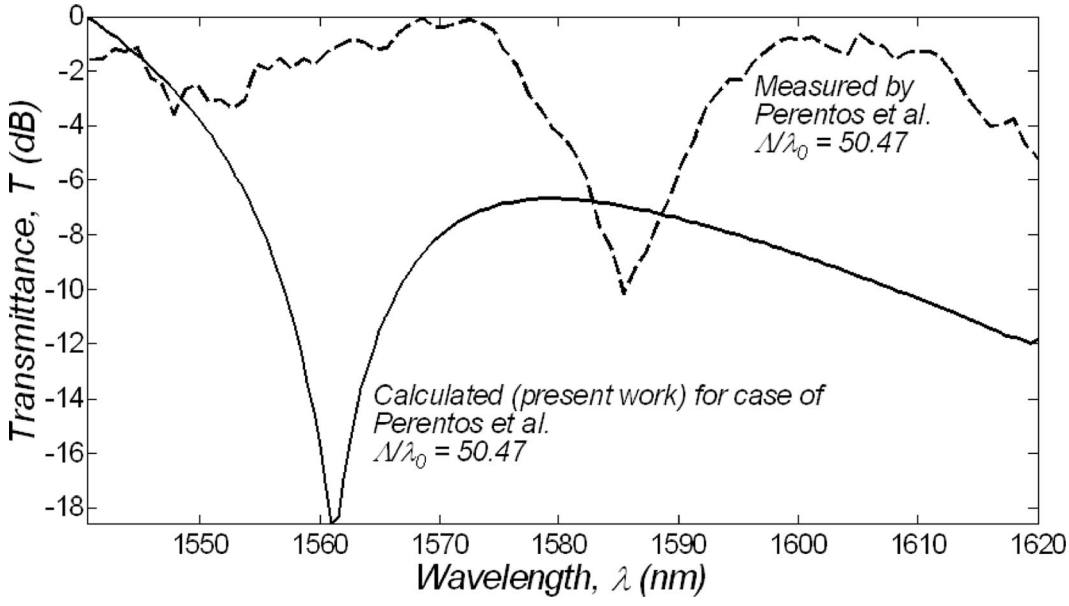

Fig. 5. Comparison between the present computed transmittance and experimental transmittance of Perentos *et al.* (Ref. 16).

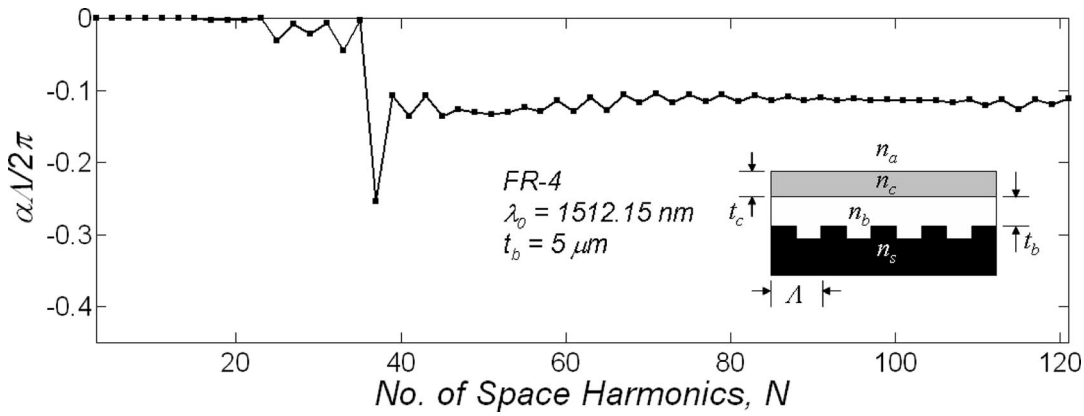

Fig. 6. Variation of the normalized attenuation constant ($\alpha\Lambda/2\pi$) versus the number of space harmonics employed for the structure shown as an inset. The inset is the simplified waveguide-on-PCB structure under investigation with $n_a = 1.0$, $n_c = 1.525$, $n_b = 1.49$, $n_s = 3.47$, $t_c = 10$ μm, and $t_b = 5$ μm. The convergence test is intentionally conducted for the attenuation constant in the stop band where the normalized frequency Λ/λ_0 is 264.53.

20 μm thick UV15 buffer layer. The number of space harmonics used in the calculation was 41. Good agreement can be seen in terms of the resonance wavelength where the computational result is 1.51% deviated from the measured resonance peak at $\lambda_0 = 1585$ nm. The discrepancies between the experimental data and the theoretical analysis may be attributed to (1) the deviation of the 2D boundary-value problem from the 3D physical structure where the raised-rib waveguide was treated as a slab waveguide and (2) the assumption of an infinite periodic boundary in the mathematical formulations given in Eq. (5).

The convergence test of the attenuation constant normalized to the grating period, $\alpha\Lambda/2\pi$, versus the truncation order for the FR-4 substrate undulations is given in Fig. 6. The structure under investigation is depicted as the inset in the figure and will be used in the calculations of the normalized attenuation constant hereafter. For simplicity, the substrate undulations are approximated by a layer of rectangular corrugations with a fill factor of 0.5. The fill factor of 0.5 was chosen to better represent the sinusoidal nature of the real undulations in FR-4 buildup boards. The FR-4 substrate grating has a period of 400 μm and a corrugation depth of 8 μm, which is the largest measured value for FR-4 PCBs. The bulk refractive indices of the waveguide core (n_c), buffer layer (n_b), and substrate (n_s) are 1.525, 1.49, and $\sqrt{4.4}$, respectively. The normalized frequency Λ/λ_0 was intentionally chosen at 264.5284 with a buffer layer of 5 μm for obtaining the complex dispersion root in the stop band. The number of space harmonics employed ranges from 3 to 121 and the behavior of the normalized attenuation constant of the fundamental mode is examined. The $\alpha\Lambda/2\pi$ value settles down within a variation of 0.03 for $N > 40$ and appears to converge well as the number of space harmonics exceeds 60 at which the minimum normalized amplitude of space

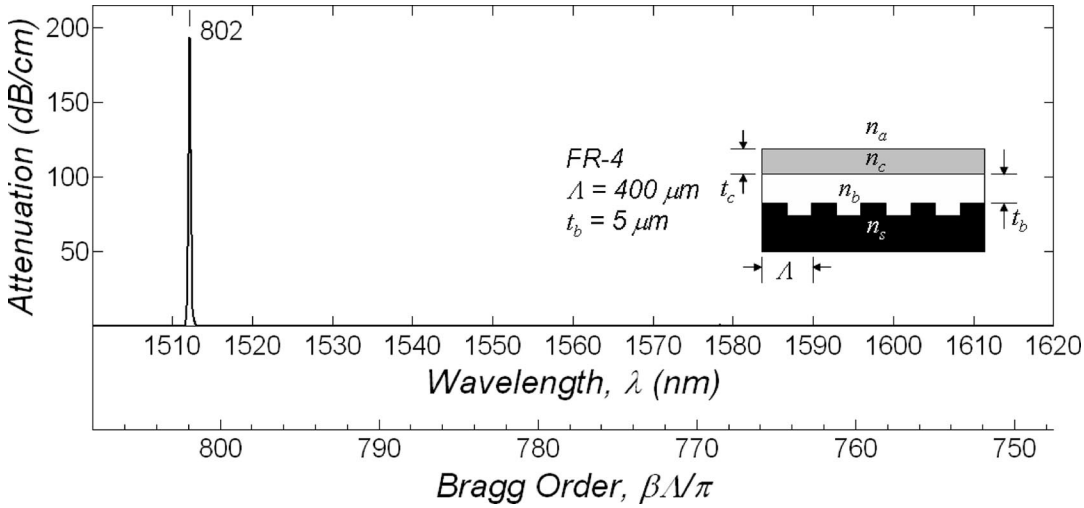

Fig. 7. Attenuation spectra of a polymer slab waveguide fabricated on bare FR-4 PCB where long-period undulations are present. The inset is the simplified waveguide-on-PCB structure under investigation with $n_a = 1.0$, $n_c = 1.525$, $n_b = 1.49$, $n_s = 3.47$, $t_c = 10$ μm, and $t_b = 5$ μm.

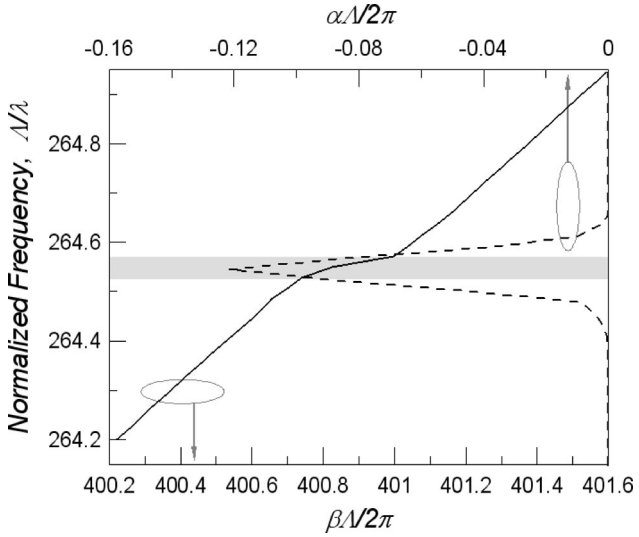

Fig. 8. Magnification of the dispersion curve in the vicinity of $\beta\Lambda/2\pi = 401$ for the attenuation peak shown in Fig. 7. $\beta\Lambda/2\pi$ and $\alpha\Lambda/2\pi$ denote the normalized propagation and attenuation constants, respectively. Note that the corresponding Bragg condition $\beta\Lambda/2\pi$ is 802.

harmonics is well below 10^{-5} in Fig. 3. Although the convergence test involves a complicated complex root finding process through the dispersion relation that is structure dependent, the abrupt step shown in Fig. 6 may be physically understood as being a starting condition where the number of terms in the Fourier series expansion of the given rectangular corrugations is large enough to better describe the abrupt discontinuities. The attenuation constants found with a smaller number of space harmonics ($N < 41$) are thus not trustworthy. Moreover, because of the long-period Λ, the space harmonics that are physically significant are densely populated at approximately $n = 0$ order in the infinite range of harmonic n and thus must be retained in the truncated matrices. As a result, the propagation constant difference between adjacent propagating order (space harmonic) is very small and having sufficient coverage of significant orders, which is structure dependent, needs a larger number of space harmonics to be employed.

The TE_0 guided-mode attenuations due to the long-period FR-4 substrate grating for various buffer layer thicknesses are shown in Figs. 7–10. The second x axis is the corresponding Bragg order for $\Lambda = 400$ μm and the wavelength range presented. To investigate the effect of the buffer layer thickness, its thickness was varied while other geometric and material parameters remained unchanged. The core layer thickness (t_c) is set to 10 μm. The buffer layer thickness (t_b) is assumed to be 5, 20, and 40 μm measured from the top of the corrugations. For the 5 μm case, a very large attenuation may occur at $\lambda_0 \cong 1512$ nm, corresponding to the Bragg order ($\beta\Lambda/\pi$) of 802. It should be noted that the large Bragg order is due to the large period of FR-4 surface undulations. Figure 8 depicts the magnification of the dispersion curve in the vicinity of the Bragg order of 802 as a mutual verification of the calculation shown in Fig. 7. The vertical axes at the left- and right-hand sides represent the normalized frequency Λ/λ_0 while the upper and lower horizontal axes denote the normalized attenuation $\alpha\Lambda/2\pi$ and phase $\beta\Lambda/2\pi$ constant, respectively. The attenuation peak occurs at $\beta\Lambda/2\pi = 400.9975$ and is thus very close to the Bragg order of 802. The attenuation constant $\alpha\Lambda/2\pi$ varies over the nonvertical gap marked by the shaded strip. It remains nonzero in the vicinity outside of the nonvertical stop band and decreases as the $\beta\Lambda/2\pi$ deviates from 401 (or equivalently, from the Bragg order of 802), suggesting that the leakage occurs continuously before and after the near-Bragg order. The nonvertical gap shown in Fig. 8 is therefore recognized as a leaky-wave stop band. The FR-4 substrate grating diffracts the fundamental mode to another leaky

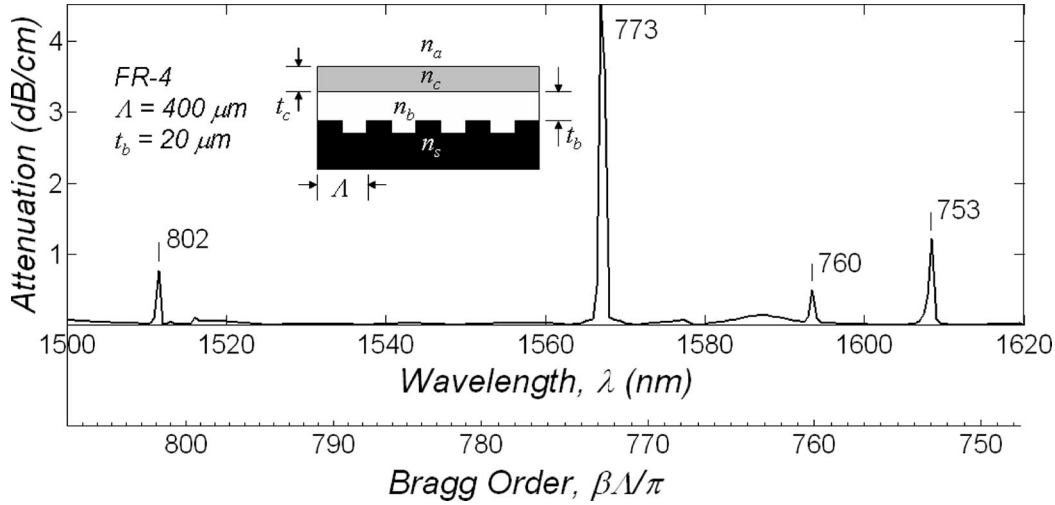

Fig. 9. Attenuation spectra of a polymer slab waveguide fabricated on bare FR-4 PCB where long-period undulations are present. The inset is the simplified waveguide-on-PCB structure under investigation with $n_a = 1.0$, $n_c = 1.525$, $n_b = 1.49$, $n_s = 3.47$, $t_c = 10$ μm, and $t_b = 20$ μm.

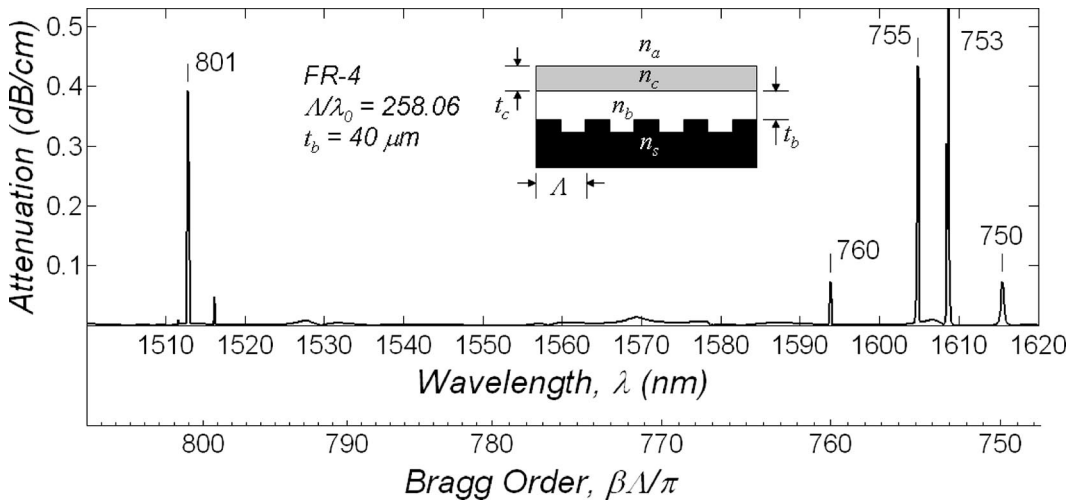

Fig. 10. Attenuation spectra of a polymer slab waveguide fabricated on bare FR-4 PCB where long-period undulations are present. The inset is the simplified waveguide-on-PCB structure under investigation with $n_a = 1.0$, $n_c = 1.525$, $n_b = 1.49$, $n_s = 3.47$, $t_c = 10$ μm, and $t_b = 40$ μm.

cladding mode (or equivalently, space harmonic) when the Bragg condition is nearly satisfied. More specifically, the attenuation may result from the contraflow interaction (coupling) between the backward-propagating fundamental mode and the cladding mode supported by the entire structure. Although, intuitively, the reflection could hardly occur with a large-period grating, it is plausible in the computation in that the substrate grating is assumed to be infinite in extent.

While only one attenuation maximum is found for a buffer layer of 5 μm, attenuation peaks in a few decibel range could be found at some specific wavelengths in the wavelength span from 1620 to 1550 nm for a 20 μm thick buffer layer. The peaks of attenuation also occur at the near-Bragg conditions. The βλ values are very close to 753π, 760π, 773π, and 802π, respectively, rather than exactly at those values. With a 40 μm thick buffer layer, the attenuation becomes even smaller over the wavelength range of interest compared with that for the 5 or 20 μm thick buffer layer. With the increase of buffer layer thickness, more leaky cladding modes can be supported by the structure. Thus more leaky-wave stop bands would occur at other wavelengths for the 40 μm thick buffer layer, in addition to those for both the 5 μm (Fig. 7) and 20 μm cases (Fig. 9). Since the perturbation introduced by the periodic undulations to the guided modes dwindles as the buffer layer thickness increases, the decreasing attenuation constant could be attributed to the weak grating-assisted couplings.

5. Conclusions

The guided-mode attenuation on FR-4 PCBs due to long-period substrate undulations has been rigorously analyzed and quantified as a function of the buffer layer thickness. The rigorous transmission-line network approach is employed to model as a 2D boundary-value problem of a dielectric waveguide on a long-period substrate grating. The number of space harmonics needed for obtaining convergent dispersion roots, either for the short- or long-period cases, can be quantitatively estimated by calculating the minimum normalized amplitude of the space harmonics. The results show that more space harmonics are required for long-period structures compared with short-period ones. Further, for long-period cases, TM polarization requires more space harmonics than does TE polarization. The results show that for a 20 μm thick buffer layer on a rectangular corrugated FR-4 substrate having a period of 400 μm and a corrugation depth of 8 μm, the attenuation is about 4 dB/cm at some specific wavelength near 1550 nm. These attenuation peaks correspond to near-Bragg points where the leakage occurs continuously in the vicinity of the Bragg points. Hence the attenuation peak corresponds to the leaky-wave stop band. As the buffer layer thickness increases, the attenuation becomes negligibly small, which is attributed to the weak grating-induced perturbation to the mode behavior. Thus a better understanding of one of the causes of guided-mode attenuation associated with the on-board polymer waveguide for board-level optical interconnects has been presented.

References

1. D. A. B. Miller and H. M. Ozaktas, "Limit to the bit-rate capacity of electrical interconnects from the aspect ratio of the system architecture," J. Parallel Distrib. Comput. **41,** 42–52 (1997).
2. D. Huang, T. Sze, A. Landin, R. Lytel, and H. L. Davidson, "Optical interconnects: Out of the box forever?" IEEE J. Select. Topics Quantum Electron. **9,** 614–623 (2003).
3. R. T. Chen, L. Lin, C. Choi, Y. J. Liu, B. Bihari, L. Wu, S. Tang, R. Wickman, B. Picor, M. K. Hibbs-Brenner, J. Bristow, and Y. S. Liu, "Fully embedded board-level guided-wave optoelectronic interconnects," Proc. IEEE **88,** 780–793 (2000).
4. E.-H. Lee, S. G. Lee, B. H. O, S. G. Park, and K. H. Kim, "Fabrication of a hybrid electrical-optical printed circuit board (EO-PCB) by lamination of an optical printed circuit board

(O-PCB) and an electrical printed circuit board (E-PCB)," in Proc. SPIE **6126,** 215–224 (2006).
5. Y. Ishii, S. Koike, Y. Arai, and Y. Ando, "SMT-compatible large-tolerance 'opto-bump' interface for interchip optical interconnections," IEEE Trans. Adv. Packag. **26,** 122–127 (2003).
6. G.-K. Chang, D. Guidotti, F. Liu, Y.-J. Chang, Z. Huang, V. Sundaram, D. Balaraman, S. Hegde, and R. Tummala, "Chip-to-chip optoelectronics SOP on organic boards or packages," IEEE Trans. Adv. Packag. **23,** 386–397 (2004).
7. L. Schares, C. Schow, F. Doany, C. Schuster, J. Kash, D. Kuchta, P. Pepeljugoski, J. Schaub, J. Trewhella, C. Baks, R. John, L. Shan, S. Hegde, Y. Kwark, D. Rogers, F. Libsch, R. Budd, P. Chiniwalla, J. Rosner, C. Tsang, C. Patel, D. Kucharski, D. Guckenberger, R. Dangel, B. Offrein, M. Tan, G. Trott, A. Nystrom, A. Tandon, C. K. Lin, and D. Dolf, "'Terabus'—a waveguide-based parallel optical interconnect for Tb/s-class on-board data transfers in computer systems," in *31st European Conference on Optical Communications* (*ECOC*) *2005* (IEE, 2005), Vol. 3, pp. 369–372.
8. V. Rastogi and K. S. Chiang, "Long-period gratings in planar optical waveguides," Appl. Opt. **41,** 6351–6355 (2002).
9. K. S. Chiang, K. P. Lor, C. K. Chow, H. P. Chan, V. Rastogi, and Y. M. Chu, "Widely tunable long-period gratings fabricated in polymer-clad ion-exchanged glass waveguides," IEEE Photon. Technol. Lett. **15,** 1094–1096 (2003).
10. K. S. Chiang, C. K. Chow, H. P. Chan, Q. Liu, and K. P. Lor, "Widely tunable polymer long-period waveguide grating with polarization-insensitive resonance wavelength," Electron. Lett. **40,** 422–423 (2004).
11. K. P. Lor, Q. Liu, and K. S. Chiang, "UV-written long-period gratings on polymer waveguides," IEEE Photon. Technol. Lett. **17,** 594–596 (2005).
12. Q. Liu, K. S. Chiang, K. P. Lor, and C. K. Chow, "Temperature sensitivity of a long-period waveguide grating in a channel waveguide," Appl. Phys. Lett. **86,** 241 115 (2005).
13. M.-S. Kwon and S.-Y. Shin, "Tunable polymer waveguide notch filter using a thermooptic long-period grating," IEEE Photon. Technol. Lett. **17,** 145–147 (2005).
14. A. M. Vengsarkar, P. J. Lemaire, J. B. Judkins, V. Bhatia, T. Erdogan, and J. E. Sipe, "Long-period fiber gratings as band-rejection filters," J. Lightwave Technol. **14,** 58–65 (1996).
15. H. C. Tsoi, W. H. Wong, and E. Y. B. Pun, "Polymeric long-period waveguide gratings," IEEE Photon. Technol. Lett. **15,** 721–723 (2003).
16. A. Perentos, G. Kostovski, and A. Mitchell, "Polymer long-period raised rib waveguide gratings using nano-imprint lithography," IEEE Photon. Technol. Lett. **17,** 2595–2597 (2005).
17. Q. Liu, K. S. Chiang, and V. Rastogi, "Analysis of corrugated long-period gratings in slab waveguides and their polarization dependence," J. Lightwave Technol. **21,** 3399–3405 (2003).
18. S. T. Peng, T. Tamir, and H. L. Bertoni, "Theory of periodic dielectric waveguides," IEEE Trans. Microwave Theory Tech. **23,** 123–133 (1975).
19. T. Tamir and S. Zhang, "Modal transmission-line theory of multilayered grating structures," J. Lightwave Technol. **14,** 914–927 (1996).
20. L. Yan, M. Jiang, T. Tamir, and K.-K. Choi, "Electromagnetic modeling of quantum-well photodetectors containing diffractive elements," IEEE J. Quantum Electron. **35,** 1870–1877 (1999).
21. M. Jiang, T. Tamir, and S. Zhang, "Modal theory of diffraction by multilayered gratings containing dielectric and metallic components," J. Opt. Soc. Am. A **18,** 807–820 (2001).
22. S. T. Peng, "Rigorous formulation of scattering and guidance by dielectric grating waveguides: general case of oblique incidence," J. Opt. Soc. Am. A **6,** 1869–1883 (1989).